Effects of Atmospheric Thermal Stability and Slope Steepness on the Development of Daytime Thermally Induced Upslope Flow

Z. J. YE,* M. SEGAL AND R. A. PIELKE

Department of Atmospheric Science, Colorado State University, Fort Collins, CO 80523

(Manuscript received 6 November 1986, in final form 1 May 1987)

ABSTRACT

The impact of background atmospheric thermal stability and slope steepness on the daytime thermally induced upslope flows was investigated using analytical and numerical model approaches. The study focuses on meso-β domains and considers the noon and early afternoon period in which, in general, steady-state flows typically occur during synoptically undisturbed days. The conclusions obtained with the analytical and numerical evaluations agreed. It was concluded that the maximum intensity of the upslope flow is generally not dependent on the background atmospheric stability. Its relation to the amount of thermal heating and slope steepness is evaluated. The steady-state characteristics of the daytime induced upslope flows were also evaluated.

1. Introduction

In many situations, daytime induced thermal circulations along mountain slopes play a major role in determining local weather and pollution dispersion. Numerous observational and modeling studies have been carried out to evaluate these circulations. Defant (1951), for instance, reviewed the state of understanding of these circulations at that time. He provided a classical schematic illustration of the diurnal cycle of thermal circulation. In the following years, observational studies (e.g., MacHattie, 1968; Whiteman and McKee, 1977; Banta and Cotton, 1981; Whiteman and McKee, 1982; Banta, 1984; Toth and Johnson, 1985; among others) have provided further observational refinements into the characteristics of these flows. Numerical model studies, such as Orville (1964), Mahrer and Pielke (1977), Mannouji (1982), Bader and McKee (1983), Tang and Peng (1983), and Banta (1984), among others, have also enhanced our understanding of these systems. Generally, however, relatively little focused attention has been given in studies during the recent three decades to a specific evaluation of the relationship between the atmospheric background thermal stability, the slope steepness and the generation of these flows. The existing classical evaluation of these relationships is provided in Prandtl's (1942) simplified model solution. Some improvements to Prandtl's solution are reported by Gutman and Melgarejo (1981) and Sorbjan (1983). However, as pointed out by Atkinson (1981), in general there is a sparsity of theoretical work on thermally induced upslope winds, while the effect of thermal stability on slope winds is unaddressed.

It is the purpose of the present study to further explore and refine the relationship between atmospheric background stability, slope steepness and thermally induced upslope flow (assuming negligible synoptic flow), using an improved linear analytical procedure as well as numerical model simulations. In the present study the slope steepnesses were assumed to be less than 5° in order to reasonably satisfy constraints required by the linear solution. The slope steepnesses considered in the study are involved with meso-β scales (i.e., horizontal domain scale 20–200 km). Solutions involved with the analytical methodology are presented in section 2. Details relating to the numerical mesoscale model used in the present study are given in section 3. A summary of results obtained using the analytical and the numerical model approaches is presented in section 4. Finally, the study focuses on situations involved with a uniform background thermal stratification in the lower atmosphere. It emphasizes the noon and early afternoon hours in which the upslope winds usually reach their peak values and are close to steady state. Evaluations of the time scale needed in order to establish steady-state upslope flow are provided in section 4c.

2. Analytical methodology

The classical solution of the daytime thermally induced upslope flow by Prandtl (e.g., see Defant, 1951) is based on the assumption that the slope is infinite in its length, the perturbation of the potential temperature on the slope surface is uniform along the slope, the Coriolis effect is neglected, and nonlinear advective effects are ignored. The resultant linear equations for the

* On leave from Institute of Atmospheric Physics, Academica Sinica, Beijing, China.

tendencies of the thermally induced upslope wind component u' and the perturbation in potential temperature, θ', from the background values (the Prandtl model equations) are

$$\frac{\partial u'}{\partial t} = \lambda\theta' \sin\alpha + \frac{\partial}{\partial z} K \frac{\partial u'}{\partial z} \tag{1}$$

$$\frac{\partial \theta'}{\partial t} = -\beta_0 u' \sin\alpha + \frac{\partial}{\partial z} K \frac{\partial \theta'}{\partial z} \tag{2}$$

where $\lambda = g/\theta_0$, is the buoyancy parameter, $\beta_0 = \partial\theta_0/\partial z$, is the atmospheric background thermal stability, K is the vertical eddy exchange coefficient, and α is the angle of terrain slope.

The Prandtl solution of Eqs. (1) and (2), in the steady condition through an infinitely deep atmosphere, assuming K = constant, are as follows:

$$u' = \lambda \frac{\Delta\theta}{N} \exp(-z/l) \sin(z/l) \tag{3}$$

$$\theta' = \Delta\theta \exp(-z/l) \cos(z/l) \tag{4}$$

where $\Delta\theta$ is the potential temperature perturbation along the slope surface from the free atmosphere at the same height; N is the Brunt–Väisälä frequency, $N = (\lambda\beta_0)^{1/2}$; and l is a scale height such that $l = (2K/N \sin\alpha)^{1/2} = h/\pi$, where h is the upslope depth.

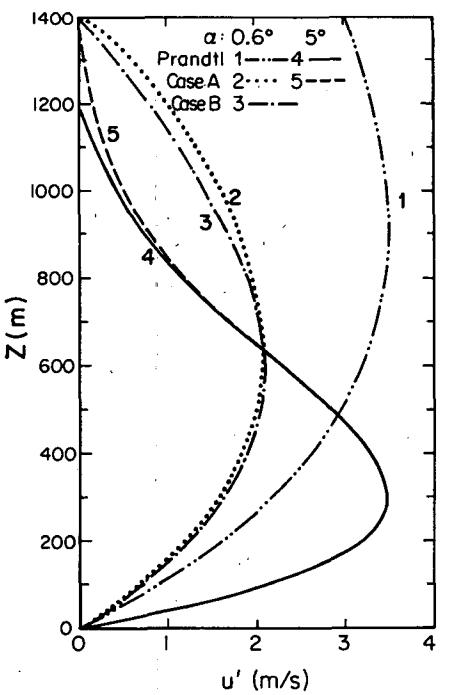

FIG. 1. Upslope wind profiles with a background thermal stability, $\beta_0 = 2.0$ K km^{-1}, $K = 50$ m^2 s^{-1} and $\Delta\theta = 2.8$ K, according to Prandtl, as well as for Case A and Case B with $h = 1414$ m with $\alpha = 0.60$ and $\alpha = 5°$.

TABLE 1. The dependence of maximum upslope wind, u'_{max}, and the height of u'_{max}, $h_{u'_{max}}$ on β_0 in the Prandtl solution and for Case A, with $\Delta\theta = 2.8$ K; $\alpha = 0.6°$, 1.2° and 5.0°; $K = 50$ m^2 s^{-1}; $h = 1414$ m for Case A.

	β_0 (K km^{-1})	1.0		2.0		4.0	
α (°)		u'_{max} (m s^{-1})	$h_{u'_{max}}$ (m)	u'_{max} (m s^{-1})	$h_{u'_{max}}$ (m)	u'_{max} (m s^{-1})	$h_{u'_{max}}$ (m)
0.6	Prandtl	5.0	1083	3.5	942	2.5	753
	Case A	2.4	659	2.1	612	1.8	565
1.2	Prandtl	5.0	706	3.5	612	2.5	471
	Case A	3.9	565	3.3	518	2.5	471
5.0	Prandtl	5.0	376	3.5	282	2.5	235
	Case A	5.0	376	3.5	282	2.5	235

Some illustrations of the Prandtl solution characteristics for daytime induced upslope flows are provided in Fig. 1. The upslope wind profiles 1 and 4 in Fig. 1, which correspond to $\alpha = 0.6°$ and 5°, respectively, were calculated according to Eq. (3) with $\beta_0 = 2.0$ K km^{-1}, $K = 50$ m^2 s^{-1}, and $\Delta\theta = 2.8$ K. In the Prandtl solution, the value of the maximum wind speed, u'_{max}, is not dependent on the slope steepness; however, the height at which u'_{max} is obtained decreases with increasing steepness. On the other hand, for a given slope, increasing the background atmospheric thermal stability, β_0, while keeping $\Delta\theta$ constant, leads to a reduction in u'_{max} as shown in Table 1.

The solution for daytime thermally induced flow along slopes suggested by Gutman and Melgarejo (1981) differs from the Prandtl solution by assuming that K varies according to the similarity theory within the surface layer and increases continuously above that layer.

In this section, additional modifications in the original Prandtl model assumptions were evaluated, in order to investigate the impact of slope steepness and atmospheric stability on daytime generated slope flows, while assuming steady-state conditions (see section 4c for estimation of the time scale needed to establish a nearly steady-state flow). Three cases, illustrating various physical aspects of upslope flow, are presented. The motivation for selection of the cases involved evaluating common assumptions applied in other studies of slope flow as well as providing more physically refined solutions. The following cases were adopted.

a. Case A: Solution is limited to the boundary layer depth

Equations (1) and (2) are solved within a limited height, h, which corresponds to the planetary boundary layer (PBL) depth instead of an infinite depth atmosphere as used in the Prandtl solution. A constant K and steady conditions are assumed within that layer (in the Prandtl solution, K is assumed to be constant

within an infinite depth). The boundary conditions imposed on Eqs. (1) and (2) are

$$u' = 0 \quad \text{at} \quad z = z_0 \quad \text{and} \quad z = h \tag{5}$$

$$\theta' = \Delta\theta \quad \text{at} \quad z = z_0 \quad \text{and} \quad \theta' = 0 \quad \text{at} \quad z = h \tag{6}$$

where z_0 is the surface roughness height (generally $z_0 \ll z$). The condition that $u' = 0$ at the top of the PBL assumes that the PBL height separates the upslope flow layer from the return flow perturbation above it. It has been indicated to be a reasonable approximation, for example, by the numerical modeling studies of Anthes (1978), Mizzi and Pielke (1984), Segal et al. (1986) and the observational study by Johnson and O'Brien (1973).

The solutions for u' and θ' under steady-state conditions are

$$u' = \lambda \frac{\Delta\theta}{N} \exp[(z_0 - z)/l] \sin[(z - z_0)/l] + \Delta u' \tag{7}$$

$$\theta' = \Delta\theta \exp[(z_0 - z)/l] \cos[(z - z_0)/l] + \Delta\theta'. \tag{8}$$

The first terms on the right-hand side of (7) and (8) are the same as the Prandtl solution given in (3) and (4), with the $\Delta u'$ and $\Delta\theta'$ terms reflecting a correction to the original Prandtl solution. A detailed derivation of (7) and (8) is provided in appendix A.

b. Case B: As Case A, except for a prescribed θ'; K is a constant with height, however, it is dependent on h

Equation (1) is solved within a boundary layer with depth, h, as with Case A. However, it is assumed that K is dependent on thermal stability through the relation $K = K_0 h$, where K_0 is a constant with units of length per time (see appendix B for details and definition of K_0). Since during the daytime the boundary layer has a bulk lapse β close to neutral, θ' can be derived from the following relation:

$$\frac{\partial\theta}{\partial z} = \frac{\partial\theta_0}{\partial z} + \frac{\partial\theta'}{\partial z} = \beta \approx 0 \tag{9}$$

where θ is the potential temperature above the slope surface. Because of the linearity involved with Prandtl's equation, the advection of θ in his solution is involved only with the background potential temperature [i.e., $(u' \sin\alpha)\partial\theta_0/\partial z$]. However, since during the daylight hours, the PBL is closely neutral (i.e., $\beta = \partial\theta/\partial z \approx 0$), the value of $|(\partial\theta'/\partial z)|$ is nearly as large as $|(\partial\theta_0/\partial z)|$. From a physical point of view, the linearity requirement in the Prandtl solution, which neglects the term $(\partial\theta'/\partial z)u' \sin\alpha$ in Eq. (2), leads to an inaccurate evaluation of the related advection within the PBL. Therefore, estimating θ' based on (9) rather than predicting it using Eq. (2), is expected to improve the accuracy of the upslope flow solution.

Using (9) and the boundary condition (6) provides the following relation for θ':

$$\theta' = \Delta\theta - \beta_0(z - z_0) \approx \beta_0(h - z) \tag{10}$$

where $\beta_0 = \partial\theta_0/\partial z$ = constant is assumed. Substituting (10) into (1) and integrating (1) with respect to z under steady condition using boundary condition (5), results in the following solution for u':

$$u' \approx \frac{\lambda \sin\alpha}{2K_0 h} z\left[\frac{\beta_0}{3}(z^2 - h^2) + (\Delta\theta + \beta_0 z_0)(h - z)\right]. \tag{11}$$

c. Case C: As Case B, except for a parabolic K profile

The equations are solved as in Case B; however, the eddy diffusion coefficient, K, has a parabolic profile within the PBL:

$$K = K_0 z(1 - z/h) \tag{12}$$

where K_0 is a constant defined in (B3) of appendix B. This type of profile has its maximum at $z = h/2$. It provides a profile that is analogous to the K profile associated with the cubic polynomial approximation suggested by O'Brien (1970) (see appendix B), which has been adopted in many boundary-layer modeling studies.

The mathematical solution in this case, assuming boundary condition (C2), is

$$u' = \frac{\lambda Q_s \sin\alpha}{2K_0}\left[\ln\left(\frac{\xi(1-\xi)}{\xi_0(1-\xi_0)}\right) - (1 - 2\xi_0) \times \frac{\ln\left(\frac{1-\xi}{\xi}\right)}{\ln\left(\frac{1-\xi_0}{\xi_0}\right)} - 2\xi + 1\right] \tag{13}$$

where

$$\xi = z/h; \quad \xi_0 = z_0/h; \quad Q_s = \frac{1}{2}h\Delta\theta.$$

A detailed derivation for this case is provided in appendix C.

3. Numerical model simulations

The analytical solutions in the previous section were derived under the assumptions that the slope is infinite and the eddy diffusion exchange coefficient has the form of a constant or a parabolic profile with height. In the real world, however, slope extent is, of course, limited. Additionally, the specification of a realistic profile of an eddy exchange coefficient, which should depend on thermal and dynamic processes, is not so simple as to be constant or parabolic. Nonlinear advective effects resolved by the numerical model could also be important. Therefore, in order to evaluate the analytical results, a set of numerical model simulations (see Table 2 for their description), designed to evaluate the impact of background atmospheric thermal stability and terrain slope on thermally induced upslope flow, was carried out. A two-dimensional hydrostatic primitive equation model was used, whose formulation is

TABLE 2. Description of the numerical model simulations.

Case	Simulation description
C1	upslope flow; summer case (15 August); background thermal stability sensitivity experiment
C2	upslope flow; summer case (15 August), slope angle sensitivity experiments; slope-plateau case
C3	upslope flow; summer case (15 August), slope angle sensitivity experiment; ridge case

given in detail in Pielke (1974), Mahrer and Pielke (1977) and McNider and Pielke (1981), and will, therefore, not be presented here.

The two-dimensional model consists of 14 vertical levels, ranging from near surface to 7 km (the model levels for potential temperature and specific humidity and related initial values are given in Table 3). Two thermal stratifications were adopted in the simulations (i) with a potential temperature gradient of 2 K km^{-1} in the lower 2500 m of the atmosphere and 3.5 K km^{-1} above this layer (which is referred to as $\beta_0 = 2$ K km^{-1}) and (ii) as in (i) but with a potential temperature lapse of 6 K km^{-1} in the lower 2500 m and 3.5 K km^{-1} aloft (referred to as $\beta_0 = 6$ K km^{-1}). The simulated domain extended horizontally for 250 km and was resolved with a grid interval of 5 km. The soil input parameters are given in Table 4.

The numerical model results for cases involved with daytime induced thermal flows along slopes have been validated successfully in various studies (e.g., Segal et al., 1982; Abbs, 1986; Abbs and Pielke, 1986; among others). These studies indicated a reasonable skill of the model in resolving flows such as those involved with the present study.

4. Analysis

a. *Dependence of upslope intensity on background thermal stability*

1) ANALYTICAL RESULTS

(i) *Comparison of Case A and Case B with the Prandtl solution.* The results for Case A, as compared to the Prandtl solutions, are given in Table 1. Generally, the presented characteristics for Case A are similar to those of Prandtl's solution: upslope maximum flow, u'_{max}, as well as its corresponding height, $h_{u'_{max}}$, reduces when the background atmospheric thermal stability, β_0, increases. The most noticeable difference between Case A and the Prandtl solution as indicated in Table 1 is computed when the slope angle is reduced and the thermal stratification approaches neutral.

Figure 1 provides additional comparisons, considering Prandtl profiles and these obtained for Case A, for slope angles 0.6° and 5° with the same $\beta_0 = 2.0$ K km^{-1} and $\Delta\theta = 2.8$ K, while assuming $h = 1414$ m for Case A. Figure 1 shows that there is almost no difference between the profiles in Case A (profile 5) and the Prandtl profile (profile 4) with $\alpha = 5°$. However, with $\alpha = 0.6°$, the Case A profile (profile 2) and the Prandtl profile (profile 1) are substantially different; the upslope flow computed by Prandtl's formulation is much stronger than that in Case A. This feature suggests that the correction of the original Prandtl solution [Eqs. (3) and (4)] through the term $\Delta u'$ in Eq. (7) becomes significant as slope steepness reduces and as thermal stability tends toward neutral. The cause of this pattern appears to be related to the possible excessive depth of the upslope flow layer, h, predicted by the Prandtl model for these situations. For example, based on the definitions of l and N and the relation $h = \pi l$ using the values $K = 50$ m^2 s^{-1}, $g/\theta = 0.03$ m s^{-2} K, $\beta_0 = 2.0$ K km^{-1} as used for the solutions of Fig. 1, the values of h are about 3500 m for $\alpha = 0.6°$ and 1210 m for $\alpha = 5°$. The value of h when $\alpha = 0.6°$ is higher than commonly observed values and is much larger than the given height, $h = 1414$ m, in Case A. However, with $\alpha = 5°$ it has nearly the same value as that in Case A.

Figure 1 also indicates that the wind profiles in Case A (profile 2) and Case B (profile 3) are similar. This is because the linear profile of θ' computed using (8) in Case A is closely identical to that derived in Case B using Eq. (10) (see Fig. 2). Figure 2 shows that in Case A the profile of θ' is nearly linear for $\alpha = 0.6°$ (profile 1), but the profile for $\alpha = 5°$ (profile 2) is nonlinear using values of β_0, $\Delta\theta$, K and h as used for Fig. 1. The difference in θ' profiles is explained by the fact that when α decreases in value (also when β_0 tends to neutral) and the vertical transport of the heat energy term, $\beta_0 u' \sin\alpha$, becomes small, as compared to the turbulent friction term $K\partial^2\theta'/\partial z^2$, assuming a steady condition, then Eq. (2) reduces to

$$K\frac{\partial^2\theta'}{\partial z^2} = 0 \tag{14}$$

TABLE 3. The numerical model levels for potential temperature and specific humidity and the related initial values.

		Level (m)													
		10	32.5	75.0	200	400	600	800	1050	1350	1750	2500	4000	6000	7000
q (g kg^{-1})		17.2	16.9	16.9	15.0	14.0	13.0	8.5	8.0	5.5	4.2	1.2	1.2	1.2	1.2
θ (K)	$\beta_0 = 2$ K km^{-1}	299.3	299.3	299.4	299.6	300.0	300.4	300.8	301.3	301.9	302.7	304.2	309.5	316.5	320.0
	$\beta_0 = 6$ K km^{-1}	299.3	299.4	299.7	300.4	301.6	302.8	304.0	305.5	307.3	309.7	314.2	319.5	326.5	330.0

TABLE 4. The soil parameters used in the numerical model simulations.

Albedo of the surface	Surface roughness	Soil conductivity	Soil density	Soil specific heat
0.2	4 cm	0.003 $cm^2 s^{-1}$	1.5 $g cm^{-3}$	1.33 J/g·deg

where (14) results in a linear solution for θ' with height. In such a situation, the profiles of u' and θ' estimated in Case A are coincident with these computed in Case B. Calculation with the values of $\Delta\theta$, K, β_0 and h used in Fig. 1 indicates that the value of $\beta_0 u' \sin\alpha$ for $\alpha = 0.6°$ is one order of magnitude less ($\sim 10^{-5}$ K s^{-1}) than that of $K\partial^2\theta'/\partial z^2$ ($\sim 10^{-4}$ K s^{-1}); however, $\beta_0 u' \times \sin\alpha$ for $\alpha = 5°$ is about the same magnitude as $K\partial^2\theta'/\partial z^2$ ($\sim 10^{-4}$ K s^{-1}).

(ii) *Upslope flow intensity as dependent on β_0, h and $\Delta\theta$.* In the following, we will discuss the impact of background thermal atmospheric stability, β_0, on the upslope flow characteristics according to Eq. (11) (i.e., Case B) when (a) $\Delta\theta$ is assumed to be a constant and (b) h is assumed to be a constant. Assumptions (a) and (b) are common in various analytical studies evaluating daytime induced upslope flows.

From Eq. (10), the height of the PBL can be approximated using $\Delta\theta$ and β_0 as

$$h \approx \Delta\theta/\beta_0. \tag{15}$$

Substituting (15) for h into (11) for small z_0 results in

$$u' \approx \frac{\lambda \sin\alpha}{6K_0}(2 - \beta_0 z/\Delta\theta)(\Delta\theta - \beta_0 z)z. \tag{16}$$

The maximum upslope wind and its corresponding height as dependent on β_0, for Case B, are

$$u'_{max} = 6.4 \times 10^{-2}\lambda \frac{(\Delta\theta)^2}{K_0\beta_0}\sin\alpha \tag{17}$$

$$h_{u'_{max}} = 0.53\Delta\theta/\beta_0. \tag{18}$$

Equations (17) and (18) indicate that for a given slope angle α, the maximum upslope wind and its corresponding height decrease with increasing β_0, while keeping $\Delta\theta$ constant. Additionally, differentiating Eq. (16) with respect to β_0 yields

$$\frac{\partial u'}{\partial \beta_0} = \frac{\lambda \sin\alpha}{6K_0} z\left(\frac{2\beta_0 z}{\Delta\theta} - 3\right) < 0. \tag{19}$$

Equation (19) shows that $\partial u'/\partial\beta_0 < 0$, since using the relation (15) results in $2\beta_0 z/\Delta\theta = (2z/h) < 3$. Namely, the magnitude of the perturbation wind speed is reduced with increasing β_0.

On the other hand, combining Eqs. (10) and (11) and eliminating $\Delta\theta$, results in

$$u' \approx \frac{\lambda \sin\alpha}{2K_0 h}\beta_0\left[\frac{(z^2 + 2h^2)}{3} - hz\right]z. \tag{20}$$

The maximum upslope wind and its corresponding height as dependent on β_0 are

$$u'_{max} \approx 6.4 \cdot 10^{-2}\lambda\beta_0 \sin\alpha \frac{h^2}{K_0} \tag{21}$$

$$h_{u'_{max}} \approx 0.53h. \tag{22}$$

Equations (20) and (21) show that for a given slope angle, the upslope wind u' and u'_{max} are proportional to β_0, when h remains constant.

The conclusions on the relation between upslope flow intensity and β_0 when $\Delta\theta$ is kept constant, Eq. (16), and when h is kept constant, Eq. (20), are apparently in contradiction. It is suggested, therefore, that a different physical parameter that relates to h and $\Delta\theta$ is needed for an adequate evaluation of upslope intensity. This requirement is outlined in the next subsection.

(iii) *Dependency of upslope intensity on β_0 and the thermal function Q_s (based on Cases B and C).* Assuming an amount of heat, Q, is injected at the surface into a unit volume of the PBL with a depth, h, results

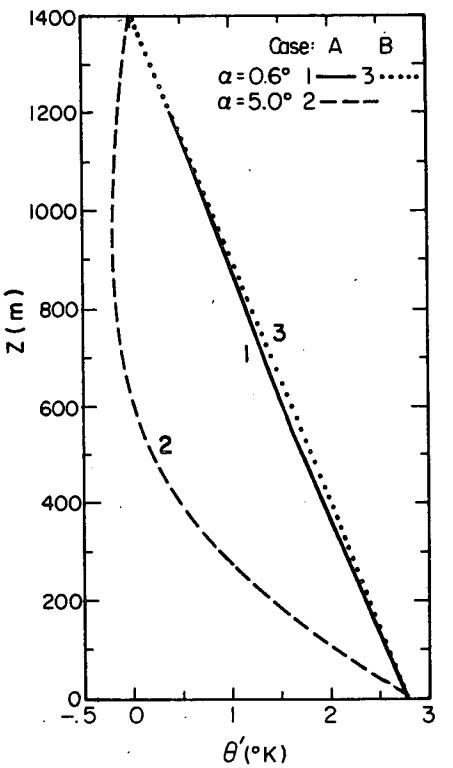

FIG. 2. Profiles of θ' as predicted by Eq. (2) (Prandtl solution) and as computed by Eq. (8) (Case B) with the same conditions as stated in Fig. 1.

in a perturbation, θ', on the potential temperature profile. The following relations then exist

$$Q = \rho C_p \int_0^h \theta' dz. \tag{23}$$

Substituting (10) into (23), and integrating (23), leads to

$$Q = \frac{1}{2}\rho C_p \beta_0 h^2, \tag{24a}$$

or

$$Q = \rho C_p (\Delta\theta)^2/(2\beta_0) \tag{24b}$$

therefore,

$$h = \left(\frac{2Q_s}{\beta_0}\right)^{1/2} \tag{25}$$

with

$$\left.\begin{aligned} \Delta\theta &= (2Q_s\beta_0)^{1/2} \\ Q_s &= Q/\rho C_p \end{aligned}\right\}. \tag{26}$$

Equations (25) and (26) suggest that both h and $\Delta\theta$ are physically functions of β_0: h is inversely proportional to $\beta_0^{1/2}$ and $\Delta\theta$ is proportional to $\beta_0^{1/2}$ for a given Q_s.

From an energetics point of view, keeping h constant and increasing β_0, as discussed in subsection (ii), means that the related thermal energy, Q, should increase according to Eq. (24a). On the other hand, keeping $\Delta\theta$ constant and increasing β_0, based on Eq. (24b), means the related thermal energy, Q, should be reduced. That is the reason for the contradictory results with respect to β_0 discussed in subsection (ii), i.e., (a) keeping $\Delta\theta$ constant and (b) keeping h constant. An adequate approach should, therefore, adopt the thermal energy source, Q, as the appropriate parameter for the evaluation of the dependence of u' on β_0.

Substituting (25) and (26) into (11), yields

$$u' \approx \frac{\lambda \sin\alpha}{K_0} Q_s \left(\frac{2+\xi^2}{3} - \xi\right)\xi \tag{27}$$

where $\xi = z/h$.

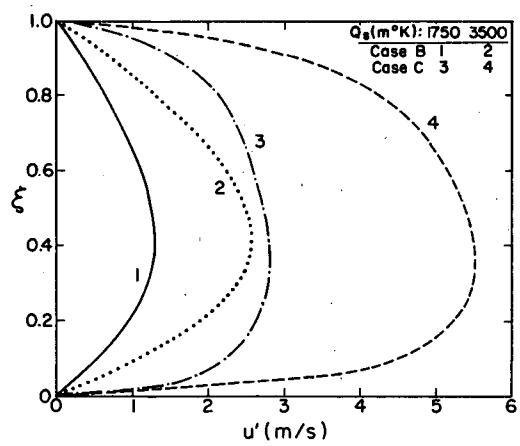

FIG. 3. The dependence of upslope flow on ξ and Q_s with α = 0.6°, and β_0 = 3.5 K km^{-1} (Case B and Case C).

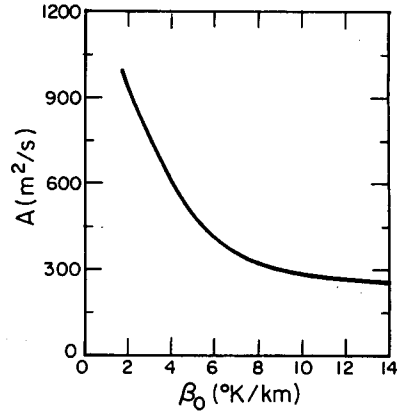

FIG. 4. The dependence of $A = \int_0^h u'dz$ [based on Eq. (30)] on the background thermal stability β_0 with α = 0.6°, K = 100 m^2 s^{-1} and Q_s = 1750 m K (Case B).

Differentiating (27) with respect to ξ and setting the result equal to zero results in

$$u'_{\max} \approx 0.13 \frac{\lambda Q_s \sin\alpha}{K_0} \tag{28}$$

$$\xi_{u'_{\max}} \approx 1 - \frac{\sqrt{3}}{3} = 0.42. \tag{29}$$

Equations (27) and (28) indicate that the upslope wind profile (in the ξ vertical coordinate) and therefore $u'_{\max}$ are dependent on Q_s. They are not, however, dependent on the background atmospheric thermal stability, β_0. This conclusion is illustrated in Fig. 3, in which profiles 1 and 2 of upslope flow for Case B are calculated with α = 0.6° and K_0 = 0.05 m s^{-1} from (27) for *any* $\beta_0 > 0$ with Q_s equal 1750 (m K) and 3500 (m K), respectively.

On the other hand, the dependence of the layer-integrated momentum of the upslope flow, $A = \int_0^h u'dz$, on the background stability β_0 is indicated by the relation:

$$A = \int_0^h u'dz = h\int_0^1 u'd\xi = S\beta_0^{-1/2} \tag{30}$$

where h was eliminated by using (25). In Eq. (30), $S = (2Q_s)^{1/2}\int_0^1 u'd\xi$, is a function of Q_s, but is independent of β_0. Consequently, Eq. (30) indicates that the layer-integrated momentum of the upslope flow, A, for a given amount of thermal energy, Q_s, is inversely proportional to $\beta_0^{1/2}$. It suggests that for a given amount of thermal energy injected at the surface into the PBL, as β_0 reduces, a higher efficiency of transformation from thermal energy into kinetic energy is obtained as shown in Fig. 4.

Equation (13) in Case C also indicates that the distribution of upslope flow, as a function of ξ, depends on the thermal energy Q_s; however, it is not dependent on β_0. Flow features in this case are shown in Fig. 3,

TABLE 5. Illustration of the relation of several characteristics of upslope flow to slope angle (α) and background thermal stability, β_0 (K km^{-1}), with Q_s = 1750 m K for Cases B and C.

Case	α (°)	u'_{max} (m s^{-1})	$h_{u'_{max}}$ (m)		h (m)	
			β_0 = 1.75	β_0 = 3.5	β_0 = 1.75	β_0 = 3.5
B	1.2	2.9	600	467	1414	1000
	0.6	1.3	600	467	1414	1000
C	1.2	5.6	518	366	1414	1000
	0.6	2.8	518	366	1414	1000

by profiles 3 [Q_s = 1750 (m K)] and 4 [Q_s = 3750 (m K)] with α = 0.6°, and K_0 = 0.8 m s^{-1}, for *any* $\beta_0 > 0$. The relationship between A and β_0 for Case C can also be expressed by Eq. (30).

A comparison of u' profiles obtained in Cases B and C (Fig. 3 and Table 5) indicates that the maximum upslope flow in the profiles corresponding to Case C (profiles 3 and 4) are about two times larger than those corresponding to Case B (profiles 1 and 2). This characteristic is caused by the fact that in Case B, where K is constant with height, the effective friction within the PBL is larger than that involved with the parabolic K applied in Case C. Table 5 was computed with the same Q_s and K as used for profiles 1 and 3 in Fig. 3. Table 5 indicates that (a) the maximum upslope flow increases as slope angle increases from 0.6° to 1.2° for both Cases B and C; (b) the height at which the upslope flow reaches its maximum, $h_{u'_{max}}$, and the depth of upslope flow, h, reduce with increasing β_0 for both Cases B and C; and (c) the value of $h_{u'_{max}}$ in Case B is higher than that in Case C; however, the u'_{max} in Case C is about two times the magnitude of that in Case B. As a result, a stronger wind shear is obtained in the lower PBL in Case C. Based on Fig. 3 and Table 5, the difference in u' profiles in the lower PBL for Cases B and C are caused as follows: the value of K in Case B is constant throughout the PBL, while in Case C, K is parabolic, leading to a larger u'_{max} and stronger wind shear in the lower part of the PBL. For example, for β_0 = 3.5 K km^{-1} and Q_s = 175 m K the K values in Case C are significantly smaller in the lower part of the PBL with a parabolic profile (K_{max} = 200 m^2 s^{-1}) as compared to the constant K profile (K = 50 m^2 s^{-1}) in Case B. Therefore, according to Eq. (1), a stronger wind shear in Case C is needed in order to reach a friction force as large as that in Case B, so as to balance the large buoyancy force near the surface (θ' is largest near the surface).

2) NUMERICAL MODEL RESULTS

In order to provide additional insight into the impact of background atmospheric thermal stability, β_0, on daytime thermally induced upslope flow, as well as an evaluation of the analytical analyses, Case C1 (commencing following sunrise) has been designed as outlined in Table 2.

Case C1 reflects a typical subtropical summer case; the soil moisture availability is 0.05 (indicating relatively dry soil), where the percent of incoming solar radiation converted to sensible heat flux is about 40 percent during the noon hours (e.g., Segal et al., 1986). Figure 5 illustrates the upslope flow in the simulated vertical cross section for 1400 LST (when the flow intensity is around its daytime peak) and shows a similar upslope flow intensity for β_0 values of 2 K km^{-1} and 6 K km^{-1}. Several typical features of the simulated upslope circulation in this case are provided in Table 6 for 1000, 1200 and 1400 LST. The numerical model results shown in Table 6 indicate that as β_0 increases, the potential temperature at the first model level, $\theta(1)$, also increases. The depth of upslope flow, $h_{u'}$, which defines the height at which the upslope wind becomes zero, is similar to the height of the PBL h_θ, which tops

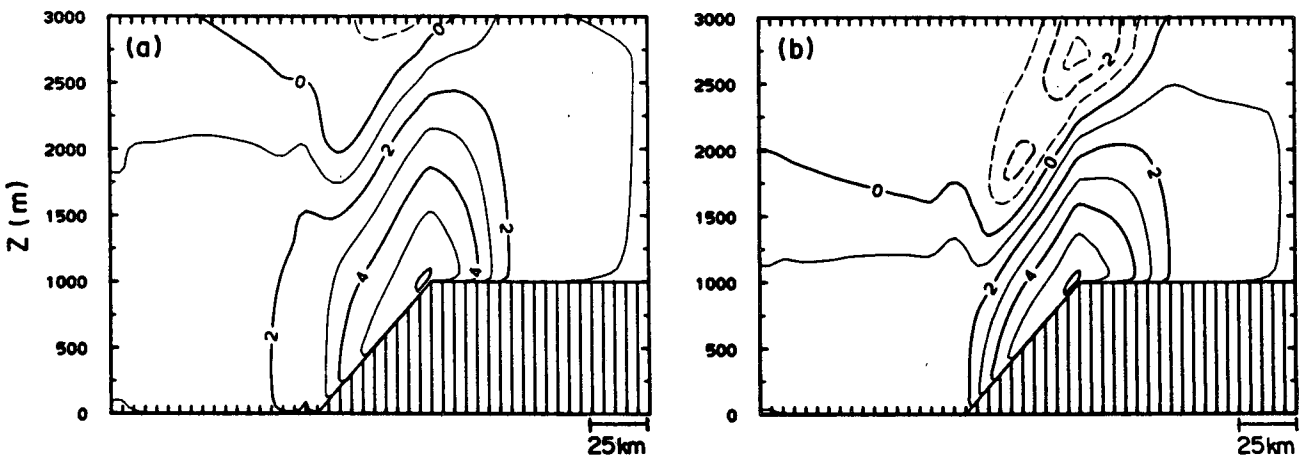

FIG. 5. Vertical cross section presenting the numerical model simulated u' for Case C1 at 1400 LST: (a) β_0 = 2 K km^{-1}; (b) β_0 = 6 K km^{-1}.

TABLE 6. Values of several pertinent parameters at the middle of the slope and for the simulated cross section (see text for their definition) as obtained from the two-dimensional simulation of Case C1. See Fig. 5 for illustration of the simulated domain terrain.

Hour (LST)	β_0 (K km^{-1})	u'_{max} (m s^{-1})	h_θ (m)	$h_{u'}$ (m)	θ (1) (K)	$\Delta\theta$ (K)	$A = \int_0^{h_{u'}} u'dz$ (m^2 s^{-1})	H_s (W m^{-2})	u^*_{max} (m s^{-1})
1000	2	3.2	1050	900	304.0	2.3	1667	284	3.4
	6	3.5	600	500	307.0	4.0	1112	269	3.7
1200	2	5.2	1750	1500	305.6	2.3	4293	354	5.4
	6	4.6	1050	900	309.3	3.4	2329	324	5.2
1400	2	5.2	2500	2000	306.6	2.1	4943	307	5.8
	6	5.5	1350	1200	310.9	3.0	3271	278	6.1

the layer in which $\partial\theta/\partial z \leqslant 0$. The sensible heat flux, H_s, is nearly equal for $\beta_0 = 2$ K km^{-1} and 6 K km^{-1}, with the depth of upslope flow much larger when $\beta_0 = 2$ K km^{-1} than when $\beta_0 = 6$ K km^{-1}. According to Eq. (25), the height of the PBL with $\beta_0 = 2$ K km^{-1} should be about 1.7 times that with $\beta_0 = 6$ K km^{-1} for the same Q_s, as closely obtained in the numerically simulated cases. The maximum upslope wind computed at the middle of the slope, u'_{max}, is also nearly constant while changing β_0, in agreement with the conclusion suggested by the analytical solutions presented previously in this paper.

The layer-integrated upslope momentum, A, for Case C1 decreases with increasing β_0; this feature is also in agreement with the analytical solutions. The values of $\Delta\theta$ [the difference between the potential temperature at the first level, $\theta(1)$, at the middle of the slope and the corresponding potential temperature at the same elevation in the free atmosphere] represent the intensity of buoyancy. Values in Table 6 show its daytime intensification. Values of u^*_{max} (the maximum upslope wind within the simulated cross section) are also presented in Table 6 and show a similarity in magnitude to u'_{max} computed at the middle of the slope.

Figure 6 presents the wind profiles above the middle of the slope at 1400 LST in Case C1. It shows that there is almost no difference in the u' profiles computed for $\beta_0 = 2$ K km^{-1} and $\beta_0 = 6$ K km^{-1}. The numerical results support the analytical results [Eqs. (13) and (27)] that the upslope flow intensity is unaffected by changes in background thermodynamic stability, β_0.

Additional general evaluations of the dependence of upslope intensity on background thermal stability are presented in subsection 4c.

b. *Thermally induced upslope dependency on slope steepness*

1) ANALYTICAL RESULTS

Computed wind speeds derived for Case A (shown in Fig. 1) and for Case B (shown in Fig. 7), as well as solutions for Case C [given by Eq. (13)], all suggest that the upslope flow intensity is proportional to sinα. Table 1 (for Case A) and Table 5 (for Cases B and C) quantitatively illustrate this relation. This relation between the intensity of the upslope flow and the slope steepness is different from the Prandtl solution, which indicates that u'_{max} does not change with terrain steepness (as can be shown analytically and as illustrated in Table 1).

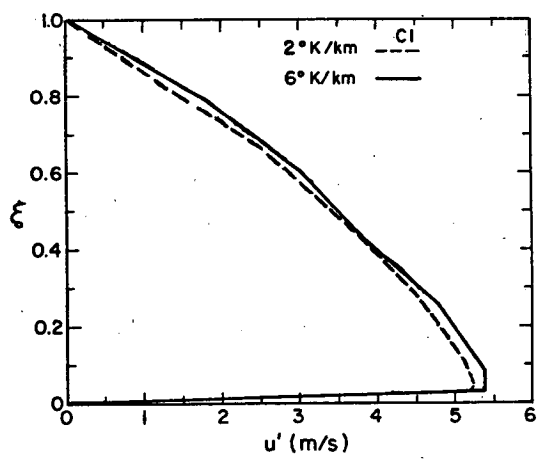

FIG. 6. Numerical model simulated vertical profiles of u' ($\xi = z/h$) at the middle of the slope at 1400 LST (Case C1).

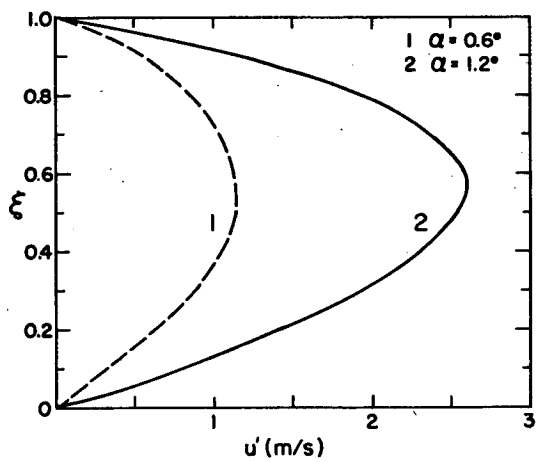

FIG. 7. Illustration of the relation of upslope flow to terrain slope angle based on Case B with $\beta_0 = 3.5$ K km^{-1}.

In the analytical derivations it was assumed that the depth of upslope flow is dependent on β_0 and $\Delta\theta$ [according to Eq. (10)] or Q_s [according to Eq. (25)], but is independent of slope steepness. This assumption is supported by the numerical model results presented in this study.

2) NUMERICAL MODEL RESULTS

Case C2 was designed to investigate the impact of slope steepness on upslope flow intensity. The horizontal extent of the slope was 50 km, while the slope steepness was changed within the range 0.23°, 0.57°, 1.15° and 2.30° corresponding, respectively, to a steepness of $1/250$, $1/100$, $1/50$ and $1/25$. The characteristics of the modeling results are listed in Table 7.

The numerical modeling results for 1400 LST show that the daytime thermally induced slope circulation intensifies when the terrain slope becomes steeper, as shown in Fig. 8 (and Fig. 5b) as well as in Fig. 9. For example, the upslope flow intensity with $\alpha = 2.3°$ ($tg\alpha = 0.04$) is 3.3 times stronger than with $\alpha = 0.23°$ ($tg\alpha = 0.004$). The u'_{max} in Fig. 9 and Table 7 and u^*_{max} values in Fig. 8 and Table 7 indicate that by doubling the terrain slope, their values increase in the range of about 20–90 percent as compared with about 100 percent for the analytical solutions. The magnitude of the increase in u'_{max} caused by a doubling of the slope is larger when the slope steepness is smaller. It appears from Table 7 and Fig. 9 that the depth of upslope flow, $h_{u'}$ is independent of the slope steepness. These numerical model results are in agreement with the results computed by the analytical solutions in the present study, but are in disagreement with those of Prandtl in which u'_{max} does not change with terrain slope and the depth of upslope flow increases with decreasing slope steepness.

Additional insight into the sensitivity of upslope induced thermal flow to the slope steepness is provided for a ridge case simulation (Case C3). A 2-D ridge with a base width of 100 km and top heights at 250, 500, 1000 and 2000 m (corresponding to $\alpha = 0.29°$, 0.57°, 1.15° and 2.30°) were simulated for the same background conditions as in Case C2. In these cases, the dependence of the upslope flow intensity on slope steepness is stronger as compared to the cases in C2, since the horizontal expansion of the thermal circulation is relatively confined and upslope flow on both sides of the ridge focuses the horizontal scale of the circulation. In C2, circulations penetrated up onto the plateau (e.g., see Atkinson, 1981; Mannouji, 1982, for the characteristics of this plateau breeze) where the extent of the penetration was related directly to the upslope flow intensity, i.e., the slope steepness. As a result, in C2 for the steep slope simulations, the flow intensity dependence on $\sin\alpha$ was less pronounced. Figure 10 illustrates the wind speed of the developed flow by 1400 LST, at the middle of the ridge slopes. Comparing to the corresponding profiles obtained in Case 2 (Fig. 9), a sharper change of the speed with slope angle is simulated for the whole range of the specified steepness. Also the flow speed closely relates linearly to $\sin\alpha$ as suggested by the analytical solution.

Further numerical modeling investigations of thermally induced upslope dependency on slope steepness are provided in subsection 4c.

c. *Time required to reach steady state*

1) ANALYTICAL EVALUATION

Substituting Eq. (10) into Eq. (1), assuming $K = K_0 h$, making the approximation for h and $\Delta\theta$ related to the sensible heat flux, H_s, as

$$\int_0^t H_s dt = \frac{1}{2}\beta_0 h^2 = \frac{\Delta\theta^2}{2\beta_0} \tag{31}$$

TABLE 7. Values of several pertinent parameters at the middle of the slope and for the simulated cross section (see text for their definition) as obtained from the two-dimensional simulation of Case C2. See Figs. 5b and 8 for illustration of the simulated domain terrain.

Hour (LST)	Slope angle α (°)	u'_{max} (m)	h_θ (m)	$h_{u'}$ (m)	θ(l) (K)	$\Delta\theta$ (K)	$A = \int_0^{h_{u'}} u'dz$ ($m^2\ s^{-1}$)	H_s ($W\ m^{-2}$)	u^*_{max} ($m\ s^{-1}$)
1000	2.30	4.4	600	500	309.1	3.5	1448	280	5.0
	1.15	3.5	600	500	307.1	4.0	1112	280	3.7
	0.57	2.1	600	500	305.8	2.5	639	250	2.1
	0.23	0.9	600	500	304.8	1.3	247	250	0.9
1200	2.30	5.3	1050	900	310.9	5.2	2426	350	6.8
	1.15	4.6	1050	900	309.3	3.4	2329	350	5.2
	0.57	3.2	1050	900	308.5	2.6	1342	300	3.4
	0.23	1.5	1050	900	307.6	1.6	801	290	1.5
1400	2.30	6.2	1350	1200	312.1	4.3	3350	300	7.5
	1.15	5.5	1350	1200	310.9	3.0	3271	300	6.1
	0.57	3.8	1350	1200	310.1	2.2	2251	260	4.3
	0.23	1.9	1350	1200	309.3	1.4	1171	250	2.0

yields

$$A\frac{\partial u}{\partial t} = B\frac{\partial^2 u}{\partial \xi^2} + 1 \tag{32}$$

with the specification:

$$H_s = H_0 \sin\omega t \tag{33}$$

where

$$u = \frac{u'}{[u']}, \quad t = \frac{t}{[t]},$$

$$A = \frac{[u']}{\{[t]2\lambda(H_0\beta_0/\omega)^{1/2}(1-\xi)\sin\alpha \sin(\omega t/2)\}} \tag{34}$$

$$B = \frac{K_0}{\{4(H_0/\omega)\lambda(1-\xi)\sin\alpha \sin^2(\omega t/2)\}}, \tag{35}$$

H_0 provides the value of H_s at noon and $[t]$ is a time scale for achieving near steady state with the upslope wind speed scale $[u']$.

It is possible to evaluate the physical conditions that are involved with a near steady state of upslope flows from Eq. (32). This relation suggests that the steady-state situation is achieved when

$$A\partial u/\partial t \approx 10^{-1} \min[B\partial^2 u/\partial \xi^2, 1].$$

For near steady state, B is evaluated from Eq. (35) as on the order of 10^{-1} (assuming typical values of $H_0 = 0.3$ K m s^{-1}; $\lambda = 3.3 \times 10^{-2}$ m s^{-2} K^{-1}; $K_0 = 0.1$ m s^{-1}; $\xi = 0.5$; $\beta_0 = 3.5 \times 10^{-3}$ K m^{-1}). Therefore, based on Eq. (34), when α and β_0 decrease, the time scale $[t]$ needed for establishing a steady-state flow is longer. Referring to the slope steepness range involved with the simulations presented in subsection 4b, $[t]$ is estimated to be about 5 h with $\alpha = 2.3°$ (e.g., $\sin\alpha = 0.04$, reflecting the steep slope case in the model simulations) and $[u'] = 6$ m s^{-1}, while $[t]$ is about 11 h with $\alpha = 0.23°$ (e.g., $\sin\alpha = 0.004$, reflecting the shallow slope case in the model simulation) and $[u'] = 2$ m s^{-1}. Note that $[u']$ values were approximated based on the numerical model simulations presented in subsection 4b.

2) NUMERICAL MODEL EVALUATIONS

Simulations analogous to those described for Case C1 were carried out for combinations of various values of β_0 and α in order to examine the temporal variations of the upslope wind component (u'_{max}) at the middle of the slope (Fig. 11). The following results are indicated:

(a) In agreement with the analytical evaluations, a closely steady-state solution is obtained most rapidly with the steeper slopes, as shown in Fig. 11. With a slope angle of $\alpha = 0.23°$, a well-established steady-state solution is not obtained (Fig. 11a).

(b) In general, the tendency to establish steady-state upslope flow during the earlier hours of the day is less pronounced when the β_0 values tend toward neutral.

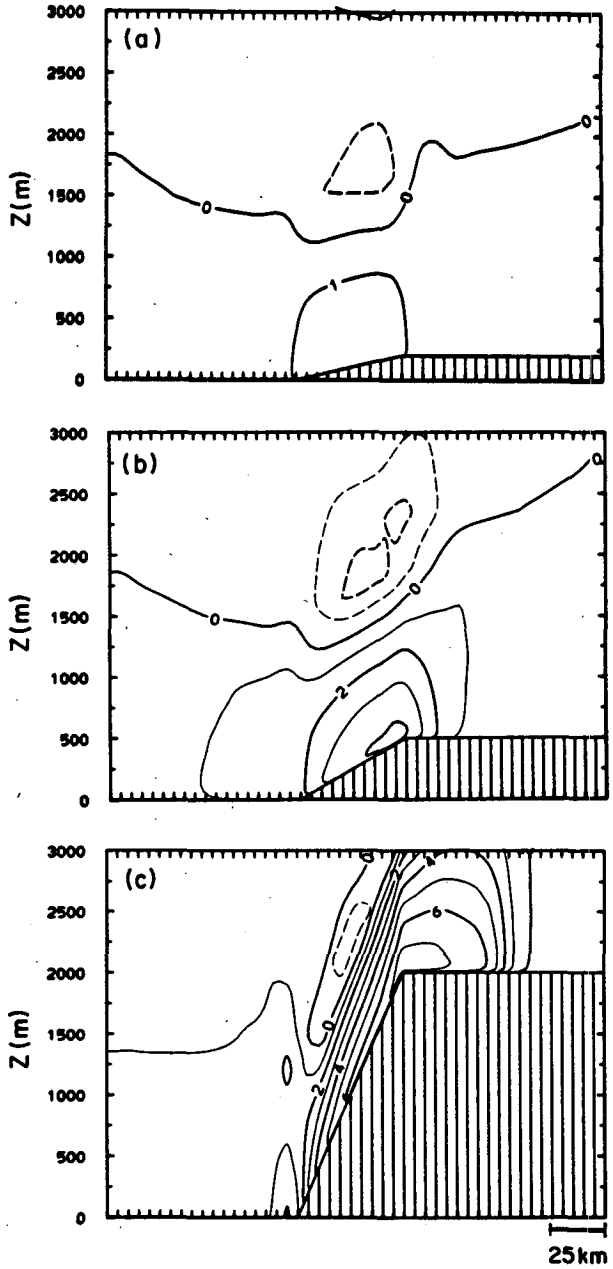

FIG. 8. Vertical cross section presenting the numerical model simulated u' for several selected slope angles: (a) 0.23°, (b) 0.57°, (c) 2.3° with $\beta_0 = 6$ K km^{-1} at 1400 LST (Case C2).

(c) Further support is provided to the general independence of the intensity of the upslope flow on β_0 (even when the upslope flow is changing with time). This independence, however, is less valid when β_0 tends toward neutral ($\beta_0 < 1$ K km^{-1}).

5. Conclusion

The present study investigated the impact of background atmospheric thermal stability and slope steep-

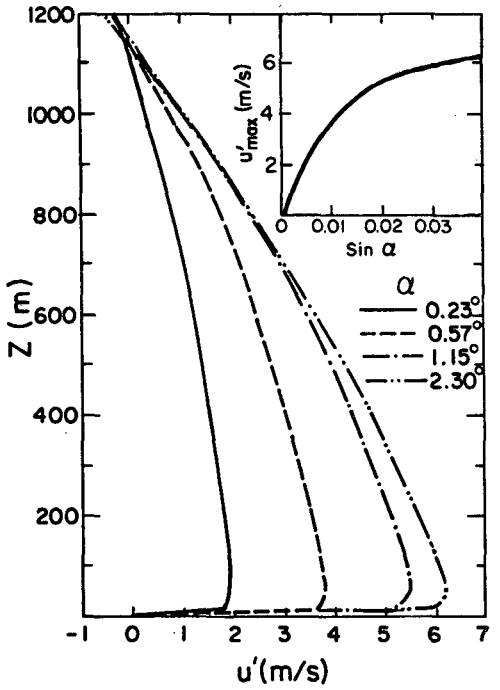

FIG. 9. Numerical model simulated vertical profiles of u' at the middle of the slope at 1400 LST for various slope angles α (Case C2). In the inset the change of u'_{max} at the middle of the slope as function of $\sin\alpha$ is presented.

ness on the daytime thermally induced upslope flow (assuming negligible synoptic flow). Slopes with a steepness of less than 5°, which are typical of meso-β

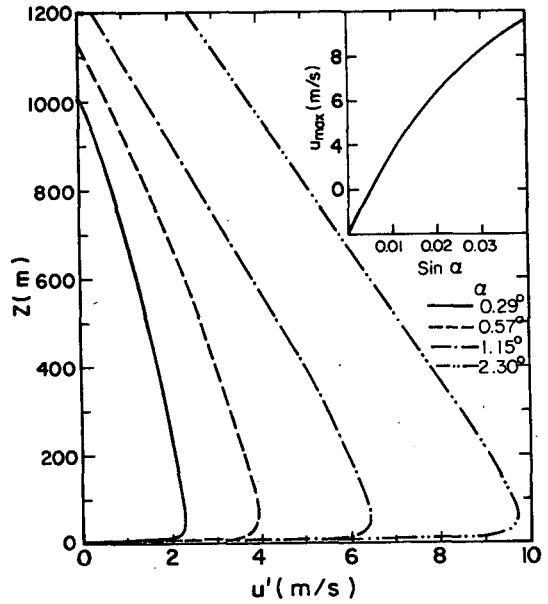

FIG. 10. Numerical model simulated vertical profiles of u' at the middle of a ridge slope (see text for definition of the selected ridges aspect ratio) at 1400 LST (Case C3). In the inset, the change of u'_{max} at the middle of the slope as a function of $\sin\alpha$ is presented.

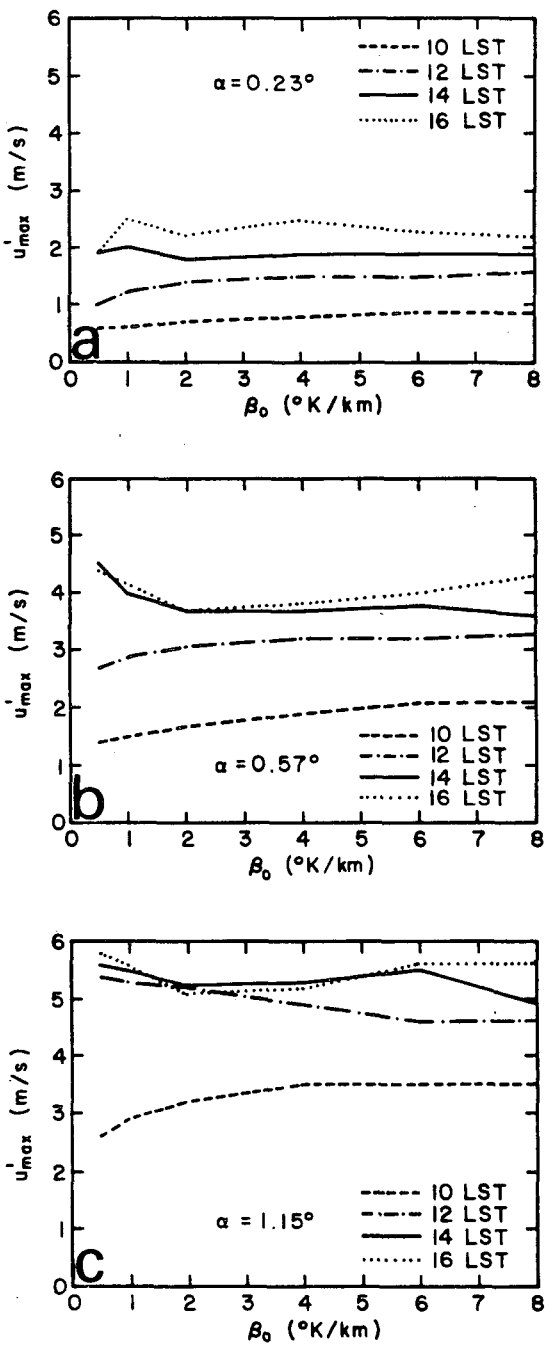

FIG. 11. Numerical model simulated values of u'_{max} at the middle of the slope as dependent on β_0 and the hour of the day, for (a) α = 0.23°, (b) α = 0.57° and (c) α = 1.15°.

domains and which satisfy the linear model constraints, were considered. Analytical solutions, including several physical refinements, were compared to the original Prandtl solution and used to develop further insight into the understanding of this thermally induced flow. Numerical simulations were carried out and contrasted with the analytical solutions.

The major conclusions of those evaluations are as follows:

(i) The daytime thermally induced upslope flow as a function of the nondimensional height, ξ, is dependent on the amount of heat energy, Q_s, injected at the surface into the PBL, and on the terrain slope, α. However, the upslope flow intensity is nearly independent of the background atmospheric thermal stability, β_0.

(ii) According to the analytical evaluation presented in this study, the intensity of upslope flow (a) increases linearly with the increase in Q_s and (b) increases linearly with respect to $\sin\alpha$. The depth of upslope flow increases when Q_s increases and/or β_0 decreases. A detailed quantitative evaluation of these relations is provided by the present study.

(iii) For a given amount of thermal energy, Q_s, the efficiency of conversion from thermal energy into kinetic energy (represented by the layer-integrated momentum of the upslope flow) increases as the background atmospheric thermal stability tends toward neutral and/or the terrain steepness increases.

(iv) General agreement between the analytical and the numerical model evaluations for the cases simulated in the present study suggest that nonlinear advective effects do not alter conclusions (i) to (iii) listed above.

Acknowledgments. This study was supported by the NSF under Grant 8414181, by the NPS under Contract NA81RAH0001, Amendment 17, Item 15, and by EPRI Grant RP-1630-53. The computations were carried out by the NCAR Computer Facility (NCAR is supported by the NSF). We would like to thank Sandra Wittler and Linda Jensen for the preparation of the manuscript and C. Dave Whiteman for his suggested improvements to the paper.

APPENDIX A

Derivation of the Solution in Case A

For the steady state, the governing equations of slope winds are as follows:

$$\frac{\partial}{\partial z}K_m\frac{\partial u'}{\partial z}+\lambda\sin\alpha\theta'=0 \tag{A1}$$

$$\frac{\partial}{\partial z}K_h\frac{\partial\theta'}{\partial z}-\beta_0\sin\alpha u'=0. \tag{A2}$$

The boundary conditions are

$$u'=0,\quad \theta'=\Delta\theta,\quad z=z_0 \tag{A3}$$

$$u'=\theta'=0,\quad z=h \tag{A4}$$

where $\lambda=g/\theta$, $\beta_0=\partial\theta_0/\partial z$, h is the height of the PBL, z_0 is the roughness of the slope surface, and $K_m=K_h=K$ is assumed. Introducing the nondimensional variables:

$$u=u'/[u'],\quad \theta=\theta'/[\theta'],$$
$$\xi=z/h,\quad K_z=K/[K]$$

where $[u']$, $[\theta']$ and $[K]$ are the scale parameters of u', θ' and K, respectively, then (A1) to (A4) can be rewritten as

$$\frac{d}{d\xi}K_z\frac{du}{d\xi}+\frac{\lambda[\theta']h^2}{[K][u']}\sin\alpha\theta=0 \tag{A5}$$

$$\frac{d}{d\xi}K_z\frac{d\theta}{d\xi}-\frac{\beta_0[u']h^2}{[K][\theta']}\sin\alpha u=0 \tag{A6}$$

$$u=0,\quad \theta=\Delta\theta/[\theta']\quad\text{at}\quad \xi=\xi_0 \tag{A7}$$

$$u=0,\quad \theta=0\quad\text{at}\quad \xi=1. \tag{A8}$$

Let

$$\eta=Nh^2\sin\alpha/[K] \tag{A9}$$

$$N=(\lambda\beta_0)^{1/2} \tag{A10}$$

and $W=\theta+iu$, then (A5) to (A8) can be rewritten as

$$\frac{d}{d\xi}K_z\frac{dW}{d\xi}+i\eta W=0 \tag{A11}$$

$$W=\Delta\theta/[\theta']\quad\text{when}\quad \xi=\xi_0 \tag{A12}$$

$$W=0\quad\text{when}\quad \xi=1. \tag{A13}$$

Assuming K_z = constant, the general solution of (A11) is

$$W=C_1\exp\left[\left(\frac{\eta}{2K_z}\right)^{1/2}(i-1)\xi\right]+C_2\exp\left[-\left(\frac{\eta}{2K_z}\right)^{1/2}(1-i)\xi\right]. \tag{A14}$$

The constants C_1 and C_2 can be written, through applying the boundary conditions (A12) and (A13), as follows:

$$C_1=\frac{\Delta\theta}{p[\theta]}\left\{\exp\left[\left(\frac{\eta}{2K_z}\right)^{1/2}(4-(1+i)\xi_0)\right]-\exp\left[\left(\frac{\eta}{2K_z}\right)^{1/2}[4+\xi_0+i(\xi_0-4)]\right]\right\}$$

$$C_2=\frac{\Delta\theta}{p[\theta]}\left\langle\exp\left[\left(\frac{\eta}{2K_z}\right)^{1/2}\xi_0(1+i)\right]-\exp\left\{\left[\left(\frac{2\eta}{K_z}\right)^{1/2}-\left(\frac{\eta}{2K_z}\right)^{1/2}\xi_0\right](1+i)\right\}\right\rangle$$

where

$$p=\exp\left[2\xi_0\left(\frac{\eta}{2K_z}\right)^{1/2}\right]+\exp\left\{2\left[\left(\frac{2\eta}{K_z}\right)^{1/2}-\left(\frac{\eta}{2K_z}\right)^{1/2}\xi_0\right]\right\}-2\exp\left[\left(\frac{2\eta}{K_z}\right)^{1/2}\right]\cos\left[\left(\frac{2\eta}{K_z}\right)^{1/2}(\xi_0-1)\right]. \tag{A15}$$

Finally, u' and θ' can be written as

$$u'=\lambda\frac{\Delta\theta}{N}\exp\left(\frac{z_0-z}{l}\right)\sin\left(\frac{z-z_0}{l}\right)+\Delta u' \tag{A16}$$

$$\theta' = \Delta\theta \exp\left(\frac{z_0 - z}{l}\right) \cos\left(\frac{z - z_0}{l}\right) + \Delta\theta' \quad \text{(A17)}$$

where

$$\Delta u' = \lambda \frac{\Delta\theta}{pN}\left[\exp\left(\frac{2h - z + z_0}{l}\right) \sin\left(\frac{2h + z - 3z_0}{l}\right) - \exp\left(\frac{2h + z - z_0}{l}\right) \sin\left(\frac{2h - z - z_0}{l}\right) - \exp\left(\frac{z + z_0}{l}\right) \sin\left(\frac{z - z_0}{l}\right) - \exp\left(\frac{3z_0 - z}{l}\right) \sin\left(\frac{z - z_0}{l}\right)\right] \quad \text{(A18)}$$

$$\Delta\theta' = \frac{\Delta\theta}{p}\left\{\exp\left(\frac{2h - z + z_0}{l}\right) \cos\left(\frac{2h + z - 3z_0}{l}\right) - \exp\left(\frac{2h + z - z_0}{l}\right) \cos\left(\frac{2h - z - z_0}{l}\right) + \left[\exp\left(\frac{z + z_0}{l}\right) - \exp\left(\frac{3z_0 - z}{l}\right)\right] \cos\left(\frac{z - z_0}{l}\right)\right\} \quad \text{(A19)}$$

and (A15) can be written as

$$p = \exp\left(\frac{2z_0}{l}\right) + \exp\left(\frac{2(2h - z_0)}{l}\right) - 2 \exp\left(\frac{2h}{l}\right) \cos\left(\frac{2(z_0 - h)}{l}\right)$$

where

$$l = \left(\frac{2K}{N \sin\alpha}\right)^{1/2}.$$

APPENDIX B

Parameterization of Eddy Exchange Coefficient

According to Pielke et al. (1983), the vertical eddy exchange coefficient $K_z(z)$ above the surface layer under unstable conditions assumes the form given by

$$K_z(z) = K_h + \left(\frac{h - z}{h - h_L}\right)^2 \left\{K_{h_L} - K_h + (z - h_L)\left[\left.\frac{\partial K}{\partial z}\right|_{h_L} + 2(K_{h_L} - K_h)/(h - h_L)\right]\right\} \quad \text{(B1)}$$

where

- h is the height of the PBL
- h_L is the height of the surface layer, assuming $h_L = h/25$
- K_h is the eddy exchange coefficient at the PBL top, assumed equal to zero
- K_{h_L} is the eddy exchange coefficient at the top of the surface layer.

If K_{h_L} is approximated by

$$K_{h_L} \approx k_0 u_* h_L,$$

which is the appropriate form if the surface layer is neutrally stratified), (B1) becomes

$$K \approx K_0 h(1 - \xi)^2\left[\frac{1}{25} + \frac{11}{12}\left(\xi - \frac{1}{25}\right)\right] \quad \text{(B2)}$$

where $\xi = z/h$, k_0 is the von Karman constant, u_* is a friction velocity, and

$$K_0 = \frac{k_0 u_*}{(0.96)^2} = 1.1 k_0 u^* \quad \text{(B3)}$$

is defined.

Equation (B2) indicates that K is proportional to h, and K is a cubic polynomial of ξ. We use $K \propto h$ in Case B and $K \propto h\xi(1 - \xi)$ in Case C as an approximation to (B2).

APPENDIX C

Derivation of the Solution in Case C

The equations and boundary conditions are as those of Case B, however, with a parabolic K profile: $K = K_0 z(1 - z/h)$. The equation for u' can be written as

$$\frac{\partial}{\partial z} K \frac{\partial u'}{\partial z} = \lambda \sin\alpha[\beta_0(z - z_0) - \Delta\theta] \quad \text{(C1)}$$

$$u' = 0 \quad \text{when} \quad z = z_0 \quad \text{and} \quad z = h - z_0. \quad \text{(C2)}$$

The general solution of (C1), which is obtained by integrating (C1), is

$$u' = \frac{\lambda h \sin\alpha}{K_0}\left[\frac{\beta_0 h}{2} \ln\left(1 - \frac{z}{h}\right) - \frac{\beta_0}{2} z - \frac{C_1}{h} \ln\left(\frac{h - z}{z}\right) + C_2\right] \quad \text{(C3)}$$

where C_1 and C_2 are integration constants.

Using the boundary conditions (C2), the constants C_1 and C_2 are expressed as

$$C_1 = \frac{\beta_0 h}{4}\left(h - \frac{2z_0 - h}{\ln[(h - z_0)/z_0]}\right) \quad \text{(C4)}$$

$$C_2 = \frac{\beta_0 h}{4}\left[1 - \ln\left(\frac{z_0(h - z_0)}{h^2}\right)\right]. \quad \text{(C5)}$$

Substituting (C4) and (C5) into (C3) yields the solution given in Eq. (13).

REFERENCES

Abbs, D. J., 1986: Sea breeze interactions along a concave coastline in southern Australia: Observations and numerical modelling study. *Mon. Wea. Rev.*, **114**, 831–846.

——, and R. A. Pielke, 1986: Thermally forced surface flow and convergence patterns over northeast Colorado. *Mon. Wea. Rev.*, **114**, 2281–2296.

Anthes, R. A., 1978: The height of the planetary boundary layer and the production of circulation in a sea breeze model. *J. Atmos. Sci.*, **35**, 1231–1239.

Atkinson, B. W., 1981: *Meso-scale Atmospheric Circulations.* Academic Press, 495 pp.

Bader, D. C., and T. B. McKee, 1983: Dynamical model simulation

of the morning boundary layer development in deep mountain valleys. *J. Climate Appl. Meteor.*, **22,** 341–351.

Banta, R. M., 1984: Daytime boundary-layer evolution over mountainous terrain. Part I: Observations of dry circulations. *Mon. Wea. Rev.*, **112,** 340–356.

——, and W. R. Cotton, 1981: An analysis of the structure of local wind systems in a broad mountain basin. *J. Appl. Meteor.*, **20,** 1255–1266.

Defant, F., 1951: Local winds. *Compendium of Meteorology,* T. F. Malone, Ed., Amer. Meteor. Soc., 655–672.

Gutman, L. N., and J. W. Melgarejo, 1981: On the laws of geostrophic drag and heat transfer over a slightly inclined terrain. *J. Atmos. Sci.*, **38,** 1714–1724.

Johnson, A., and J. J. O'Brien, 1973: A study of an Oregon sea breeze event. *J. Appl. Meteor.*, **12,** 1267–1283.

MacHattie, L. B., 1968: Kananaskis valley winds in summer. *J. Appl. Meteor.*, **7,** 348–352.

McNider, R. T., and R. A. Pielke, 1981: Diurnal boundary-layer development over sloping terrain. *J. Atmos. Sci.*, **38,** 2198–2212.

Mahrer, Y., and R. A. Pielke, 1977: A numerical study of air flow over irregular terrain. *Contrib. Atmos. Phys.*, **50,** 213–218.

Mannouji, N., 1982: A numerical experiment on the mountain and valley winds. *J. Meteor. Soc. Japan,* **60,** 1085–1105.

Mizzi, A. P., and R. A. Pielke, 1984: A numerical study of mesoscale atmospheric circulation observed during a coastal upwelling event on 23 August 1972. Part I: Sensitivity studies. *Mon. Wea. Rev.*, **110,** 1527–1534.

O'Brien, J. J., 1970: A note on the vertical structure of the eddy exchange coefficient in the planetary boundary layer. *J. Atmos. Sci.*, **27,** 1213–1215.

Orville, H. D., 1964: On mountain upslope winds. *J. Atmos. Sci.*, **21,** 622–633.

Pielke, R. A., 1974: A three-dimensional numerical model of the sea breezes over south Florida. *Mon. Wea. Rev.*, **102,** 115–139.

——, H. A. Panofsky and M. Segal, 1983: A suggested refinement for O'Brien's convective boundary layer eddy exchange coefficient formulation. *Bound.-Layer Meteor.*, **26,** 191–195.

Prandtl, L., 1942: *Fuehrer durch die Stromungslehre.* Braunschweig, Viewig und Sohn, 382 pp.

Segal, M., Y. Mahrer and R. A. Pielke, 1982: Application of a numerical mesoscale model for evaluation of seasonal persistent regional climatological patterns. *J. Appl. Meteor.*, **21,** 1754–1762.

——, J. F. W. Purdom, J. L. Song, R. A. Pielke and Y. Mahrer, 1986: Evaluation of cloud shading effects on the generation and modification of mesoscale circulations. *Mon. Wea. Rev.*, **114,** 1201–1212.

Sorbjan, S., 1983: Rossby-number similarity in the atmospheric boundary-layer heights over a slightly inclined terrain. *J. Atmos. Sci.*, **31,** 1326–1333.

Tang, W., and L. Peng, 1983: A numerical model of slopewind circulation regimes in a V-shaped valley. *Arch. Meteor. Geophys. Bioklim.*, **B32,** 361–380.

Toth, J. J., and R. H. Johnson, 1985: Summer surface flow characteristics over northeast Colorado. *Mon. Wea. Rev.*, **113,** 1458–1469.

Whiteman, C. D., and T. B. McKee, 1977: Observations of vertical atmospheric structure in a deep mountain valley. *Arch. Meteor. Geophys. Bioklim.*, **26,** 39–50.

——, and ——, 1982: Breakup of temperature inversions in deep mountain valleys: Part I. Observations. *J. Appl. Meteor.*, **21,** 270–289.